Designing and Screening Single-Atom Alloy Catalysts for CO_2 Reduction to CH_3OH via DFT and Machine Learning

Wenyu Zhou[1, 2, #], Haisong Feng[2, 3, #], Shihong Zhou[1], Mengxin Wang[1], Yuping Chen[1], Chenyang Lu[1], Hao Yuan[2], Jing Yang[2], Qun Li[1], Luxi Tan[1, *], Lichun Dong[1, *] and Yong-Wei Zhang[2, *]

[1] *School of Chemistry and Chemical Engineering, Chongqing University, Chongqing 401331, People's Republic of China*

[2] *Institute of High Performance Computing (IHPC), Agency for Science, Technology and Research (A*STAR), Singapore 138632, Republic of Singapore*

[3] *State Key Laboratory of Chemical Resource Engineering, Beijing Advanced Innovation Center for Soft Matter Science and Engineering, Beijing University of Chemical Technology, Beijing 100029, People's Republic of China*

[#] These authors contributed equally to this work.

[*]To whom correspondence should be addressed. E-mail: tanluxi@cqu.edu.cn, Lcdong72@cqu.edu.cn, and zhangyw@ihpc.a-star.edu.sg

Abstract

Carbon dioxide (CO_2) utilization technology is of great significance for achieving carbon neutrality, in which the catalytic materials play crucial roles, and among them, single-atom alloys (SAAs) are of particular interests. In this study, density functional theory (DFT) calculations and machine learning (ML) are employed to assess the effectiveness of Cu-, Ag-, and Ni-host SAAs as catalysts for electrochemical CO_2 reduction to CH_3OH. The Gibbs free energies of 477 elementary reactions across 35 SAAs involved in CO_2 reduction are calculated, and by utilizing this dataset, a trained gradient boosting regression (GBR) model is established with an excellent accuracy. Subsequently, the properties of 46 unknown SAAs are predicted, including their pathways, products, potential-determining steps (PDS), and corresponding Gibbs free energies of the PDS (G_{PDS}). Three promising candidates, ZnCu, AuAg and MoNi, stand out due to their lowest G_{PDS} among Cu-, Ag- and Ni- hosted SAAs, respectively.

Keywords: Single-atom alloys, electrochemical CO_2 reduction, density functional theory, machine learning

TOC

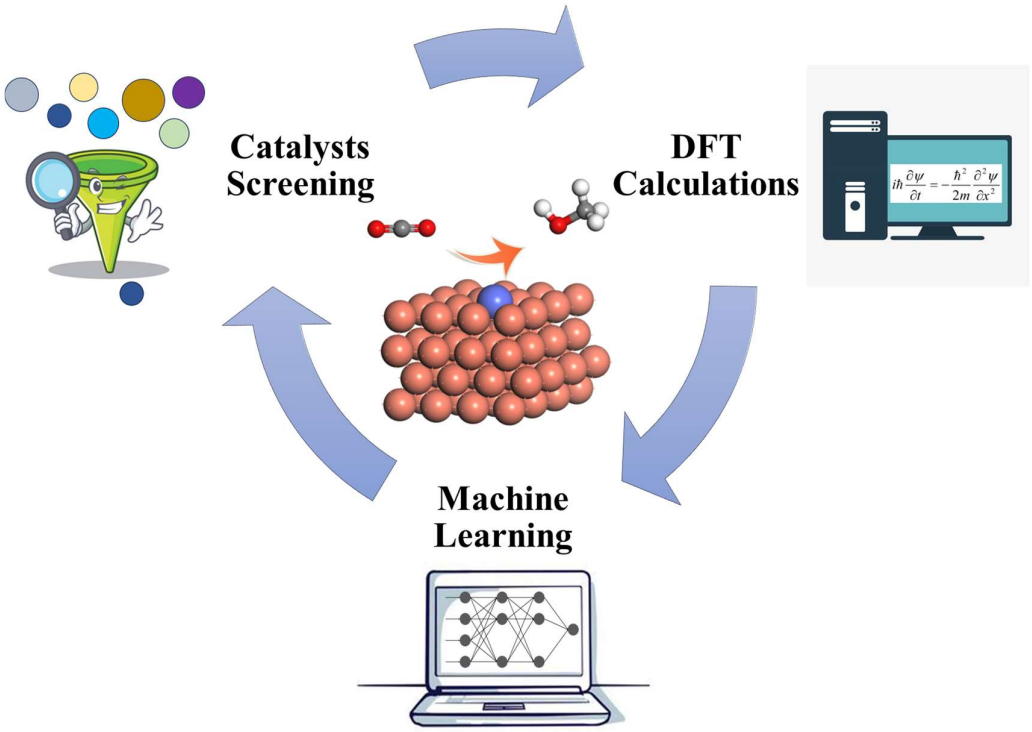

Introduction

CO_2 emissions are a significant contributor to climate change and global warming.[1-4] Consequently, carbon neutrality, also knowns as the net-zero emission, has become an urgent task and a social consensus for human society. Carbon capture, utilization and storage (CCUS) technology is of craving demand. As one of the crucial ways of CO_2 utilization, electrochemical reduction of CO_2 into HCOOH, CH_4, CH_3OH and others valuable chemicals has been achieved in lab.[4-8] However, the economy, reliability and feasibility in large scale of such process still strongly relies on the catalytic materials.

Single atom alloys (SAAs), characterized by isolated guest metal atoms dispersed on host metal atoms,[9-11] have been budding in recent years due to their excellent selectivity and activity in various chemical reactions. [12-16] Expectedly, SAAs has proven to be a strong contender in electrochemical CO_2 conversion. For instance, Zheng et al. [17] demonstrated that PbCu SAA exhibits exceptional activity in exclusively converting CO_2 into formate. Cao et al. [18] reported that BiCu SAA effectively modulates the selectivity of CO_2 reduction towards C_{2+} products instead of the traditional C_1 products. Theoretical studies on such catalytical process have also been carried out vastly by density functional theory (DFT) calculations. Zhang et al.[19] showed that PdCu SAA could effectively reduce the energy barrier of C-C coupling on the electrochemical reduction of CO_2. Neto et al.[20] discovered that doping single atoms into Ag(211)-host to form SAAs could enhance the reduction of CO_2, favoring the formation of CH_4 and CH_3OH products.

While the SAAs have already shown exciting performance, there are still a large scope of SAA combination waiting to be dogged into for the betterment of the electrochemical reduction of CO_2. Yet conducting experiments and DFT calculations both require significant resource and time. To boosting the digging process, machine learning (ML) method provides a useful tool, and make large-scale screening of catalysts possible.[2, 21, 22] Typically, ML predictions would utilize adsorption energies of certain key intermediates to determine reaction activity or selectivity. [22, 23] For example, Rittiruam et al. [22] employed adsorption energies of $*CO_2$, *CO, *COOH and *H to screen active high-entropy alloy (HEA) catalysts, and adsorption energies of *COH, $*CH_4$, *CHO and $*CH_3OH$ to identify selective HEA catalysts. Aiming at converting CO_2 to CH_3OH, Roy et al. [23] utilized adsorption energies of *H, *O, *CO, *HCO, $*H_2CO$ and $*H_3CO$ to predict selective catalysts among Cu, Co, Ni, Zn, and Mg metals in the forms of bimetallic, trimetallic, tetrametallic, and HEAs. However, the CO_2 reduction reaction is complex (Scheme 1), involving numerous potential reaction pathways. The reaction pathways and potential-determining steps (PDS) can vary across different catalysts, posing challenges in developing accurate ML models. Therefore, it is necessary to create a comprehensive dataset including Gibbs free energies, reaction pathways, and PDS data for various catalysts and reaction intermediates, covering a diverse range of catalysts, intermediates, and potential pathways. Additionally, it is also crucial to extract important, relevant features such as adsorption energies, electronic properties, geometrical parameters, and activation energies for each catalyst. These features should capture key aspects influencing the

reaction pathways and PDS. Furthermore, it is also important to select most suitable ML models by evaluating model performance on different subsets of the dataset, ensuring robustness and generalizability.

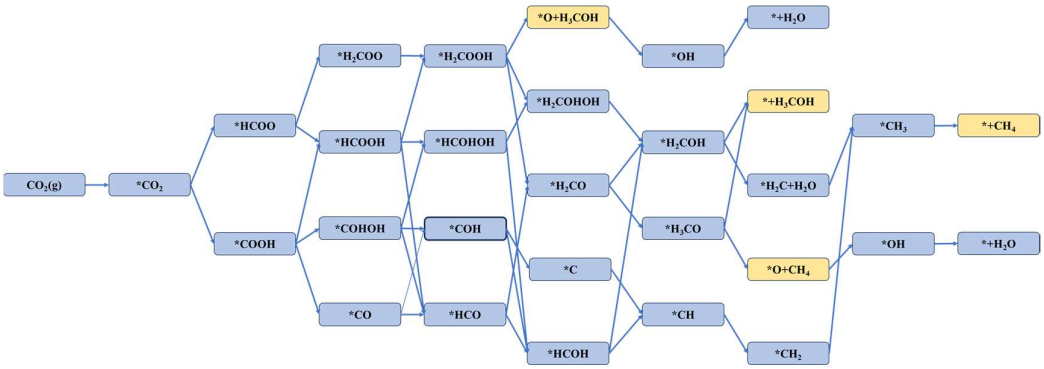

Scheme 1. The reaction pathways of CO_2 reduction to CH_3OH or CH_4. The yellow squares represent the C_1 products of CO_2 reduction.

In this study, a systematical investigation on the electrochemical reduction of CO_2 to CH_3OH on Cu-, Ag- and Ni-host SAAs with all possible transition metal doping was conducted using DFT calculations and ML (Scheme 2). DFT calculations were carried out firstly to study the reaction pathways of CO_2 reduction on 33 SAAs and pure Cu and Ni metals, yielding the Gibbs free energies of 477 elementary reactions for training an ML model. Subsequently, 6 ML models were evaluated and selected, with GBR model as the most fitting in our case. This trained GBR model was utilized to predict the Gibbs free energies of 1610 elementary reactions on 45 unknown SAAs and pure Ag metal. The CO_2 reduction reaction pathways, products, and PDS on these unknown catalysts were determined accordingly, and the most promising catalysts were

suggested and verified by DFT calculations.

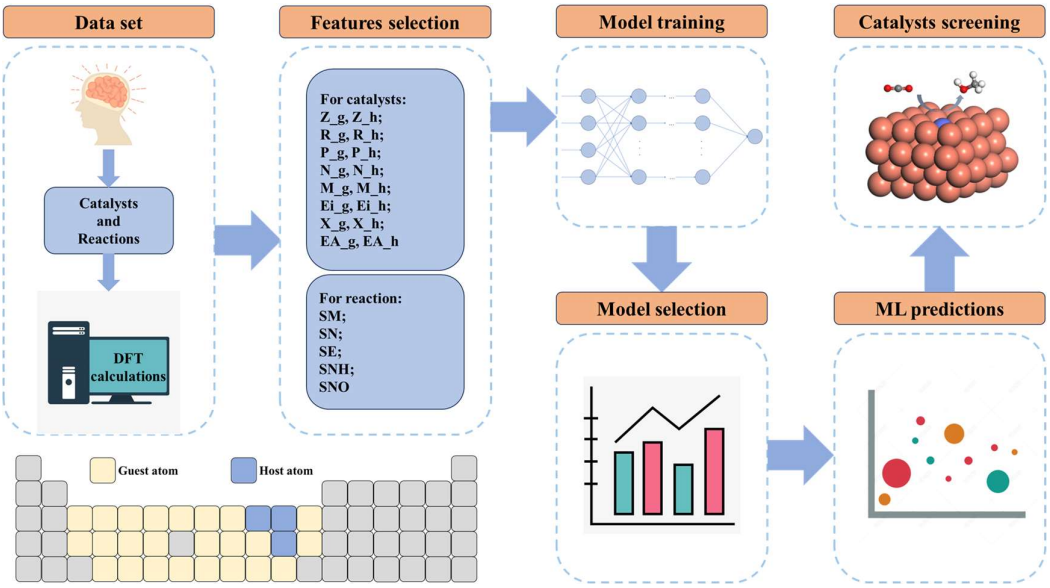

Scheme 2. Workflow for screening SAA catalysts for CO_2 reduction to CH_3OH using DFT and ML.

Methods

DFT calculations. The Vienna ab initio Simulation Package (VASP) was used to perform all of the spin-polarized DFT calculations.[24-26] The electron exchange-correlation energy was attained through the generalized gradient approximation (GGA) with Perdew-Burke-Ernzerhof (PBE) functional.[27] The plane wave energy cutoff was set as 400 eV. To generate a substantial amount of Gibbs free energy data, the calculation accuracy was slightly relaxed to reduce the calculation workload, as has been adopted in previous studies for ML predictions. [28-30] All structure optimizations were carried out with an energy convergence criterion of 1×10^{-4} eV and the forces were set as -0.05 eV/Å. The Brillouin zone was sampled using a Monkhorst-Pack k-

point mesh of 3 × 3 × 1 grid. A vacuum space of 20 Å was adopted to prevent an interaction between two adjacent images. To include the van der Waals (vdw) interactions, a dispersion correction was implemented through the DFT-D3 method.[31] To accommodate the intermediate (the maximum distance between atoms ranges from 1 to 4 Å, with CO being the smallest and H_2COHOH the largest), the 4-layer Cu(111), Ag(111) and Ni(111) slabs with a 4 × 4 supercell were built, and one Cu (Ag or Ni) atom on the topmost layer was substituted by a guest atom to model the surface of SAAs. Each supercell consisted of 64 metal atoms, including 63 host atoms and 1 guest atom. Such model size has been widely adopted in previous literatures. [32-34] The top two layers of the supercell and all adsorbates were allowed to relax fully, while the bottom two layers were fixed. In the optimized configuration presented in the Supporting Information (Figures S2-S75 and Figures S79-S82), only the topmost layer and adsorbates are shown.

The change of reaction free energy of the elementary reaction was estimated by using the computational hydrogen electrode (CHE) model, as shown in eq 1:[35-37]

$$\Delta G = \Delta E + \Delta E_{ZPE} - T\Delta S + \Delta G_{pH} + \Delta G_U \quad (1)$$

where ΔE, ΔE_{ZPE}, $T\Delta S$ represent the change of electronic energy, zero-point energy, and the entropy change at T = 298.15 K. In addition, ΔG_{pH} and $\Delta G_U = -eU$ indicate the change of free energy caused by the variation of H^+ concentration (pH = 0 under acid medium) and electrode potential (U).

More computational details are given in Supporting Information.

Machine learning. All ML algorithms were implemented using the open-source

Scikit-learn package in the *Python3* environment.[38] In this work, 6 distinct supervised ML algorithms were chosen, including Bayesian ridge regression (BRR), gradient boosting regressor (GBR), K-nearest neighbors regression (KNR), Lasso regressor (Lasso), Linear regressor (Linear) and Ridge regressor (Ridge). The objective was to develop a well-trained model capable of accurately predicting the Gibbs free energies of various elementary reactions on SAAs for CO_2 reduction. The performance of the ML model was evaluated by using the root-mean-square error (RMSE) and the coefficient of determination values (R^2 score). The RMSE and R^2 score were calculated based on eq 2 and 3, respectively:[6, 23, 28, 39]

$$RMSE = \sqrt{\frac{1}{n}\sum(y_i - \hat{y}_i)^2} \quad (2)$$

$$R^2 = 1 - \frac{\sum(y_i - \hat{y}_1)^2}{\sum(y_i - \bar{y}_1)^2} \quad (3)$$

where $\hat{y}_i$ is the ground truth, y_i is the prediction of the model and $\bar{y}_i$ is the mean value.

Results and discussion

DFT Calculations. To screen all SAAs candidates (the guest atoms include all transition atoms, except Tc, Hg and lanthanides) for electrochemical CO_2 reduction to CH_3OH, the guest atoms were randomly divided into two parts: the first part was obtained by DFT calculations, and the second part was predicted by ML. Hence, in DFT calculations, we considered a total number of 35 SAA catalysts, including Cu, Ag, and Ni as host metals, as they were often used in previous studies.[11, 15, 40-42] For guest atoms, transition metals of all periods and groups were considered. The corresponding SAAs are as follow: Sc-, Cr-, Fe-, Co-, Nb-, Ru-, Rh-, Pd-, Ag-, Ir-, Pt-, and Au-doped in Cu-host (Figure 1a); Sc-, Ni-, Cu-, Zr-, Mo-, Ru-, Ta-, W-, Re-, and Ir-doped in Ag-host

(Figure 1b); V-, Cr-, Zn-, Y-, Nb-, Ag-, Hf-, Os-, Ir-, Pt-, and Au-doped in Ni-host (Figure 1c). The pure Cu and Ni metals were regarded as special SAAs and also calculated (Figure 1a and 1c).

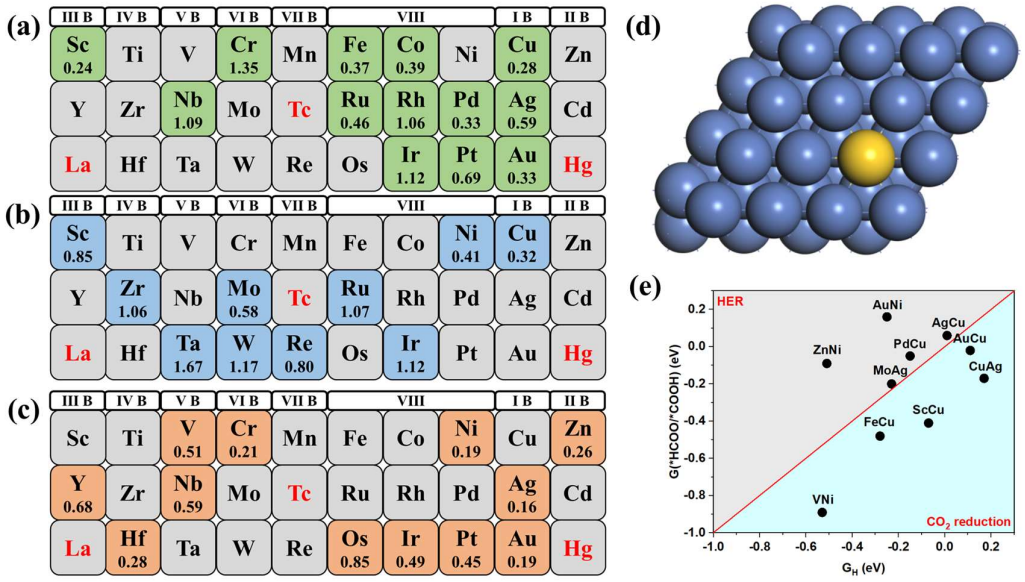

Figure 1. Transition metals doped into (a) Cu, (b) Ag and (c) Ni substrate to form SAAs. The number below the elements represents G_{PDS} (in eV) of CO_2 reduction. (d) A typical structure of SAA. The yellow and light bule balls represent the guest and host atoms, respectively. (e) Competitive comparison between HER and CO_2 reduction reaction.

For electrochemical CO_2 reduction to CH_3OH, the initial step involves CO_2 adsorption on the SAAs surfaces. All possible initial structures of CO_2 adsorption were carefully calculated, including top site, bridge sites (including CO_2 parallel and vertical to guest-host bond, referred to as bridge-p and bridge-v, respectively), hollow sites (including fcc and hcp), as illustrated in Figure S1. Following optimization, the Gibbs free energies of CO_2 adsorption (G_{ads}) on various sites were calculated and shown in Table S3. The optimal structures of CO_2 adsorption were presented in Figure S2-S4 for

Cu-, Ag- and Ni-hosted SAAs, which are in good agreement with the literature.[12] It seems that among the 35 SAA catalysts, most Ag-host SAAs show stronger adsorption capacity for CO_2, while Ni-host SAAs are weaker. Generally, the adsorption energy is determined by both guest and host atoms. [43] However, when the guest atoms are the same, the hosts become decisive. The CO_2 adsorption energy on pure host metals follows the order: Ni (0.192 eV) > Cu (0.112 eV) > Ag (0.107 eV). Hence, the general trend for the CO_2 adsorption energies on the three SAA catalysts is: Ag-host > Cu-host > Ni-host SAAs. This pattern is consistent with previous findings.[44]

Following the adsorption of CO_2, the reduction reactions were calculated, incorporating all conceivable reactions. This process entails the addition of an H atom to either C or O atom, as illustrated in Scheme 1. All the subsequent reactions were derived from the reaction in the preceding step. Both the reaction pathways and optimal structures of the intermediate results were shown in Figure S5-S30 (Cu-host SAAs), Figure S31-S50 (Ag-host SAAs) and Figure S51-S74 (Ni-host SAAs). The products, PDS, and Gibbs free energy of PDS (G_{PDS}) on different SAAs for electrochemical CO_2 reduction were summarized in Table 1 and Figure 1a-1c. For $*H_2COOH + H^+ + e^- \rightarrow *O + CH_3OH$ and $*H_3CO + H^+ + e^- \rightarrow *O + CH_4$ reactions, besides the target product CH_3OH and by-product CH_4, there remained an O atom adsorbed on the active site. It is noted that the subsequent reactions $*O \rightarrow *OH \rightarrow * + H_2O$ were studied before.[12, 13, 34, 45] From these results, it is clear that on most Cu-host and Ag-host SAAs, the CO_2 reduction reaction tends to favor the generation of CH_3OH, while on most Ni-host SAAs, it prefers to generate CH_4. Furthermore, for most SAAs that generate CH_3OH,

the reaction pathway follows CO_2 → *CO_2 → *HCOO → *HCOOH/*H_2COO → *H_2COOH → *O + CH_3OH → *OH → * + H_2O, while for most SAAs that generate CH_4, the reaction pathway follows CO_2 → *CO_2 → *COOH → *CO → *COH/*HCO → *C/*HCOH → *CH → *CH_2 → *CH_3 → * + CH_4. PDS that proceeds through the HCOO pathway predominantly involves the transition from *HCOOH to *H_2COOH, whereas PDS that goes through the COOH pathway mostly follows *CO to *COH/*HCO. We also calculated the average value of G_{PDS} for different products. It was found that the average value of G_{PDS} for CH_3OH was 0.68 eV. Therefore, SAAs with the G_{PDS} less than 0.68 eV were selected as the better electrochemical CO_2 reduction catalysts, employing a screening criterion similar to previous studies.[6, 46, 47] The results show that ScCu (G_{PDS} = 0.24 eV), FeCu (G_{PDS} = 0.37 eV), PdCu (G_{PDS} = 0.33 eV), AgCu (G_{PDS} = 0.59 eV), AuCu (G_{PDS} = 0.33 eV), CuAg (G_{PDS} = 0.32 eV), MoAg (G_{PDS} = 0.58 eV), VNi (G_{PDS} = 0.51 eV), ZnNi (G_{PDS} = 0.26 eV), and AuNi (G_{PDS} = 0.16 eV) are promising SAAs for CH_3OH production.

Table 1. The product, PDS, and G_{PDS} on different SAAs for CO_2 reduction by DFT calculated.

SAA		Product	PDS	G_{PDS} (eV)
Cu-host	pure	CH_4	*HCOOH + H^+ + e^- → *H_2COOH	0.28
	Sc	H_3COH	*OH + H^+ + e^- → * + H_2O	0.24
	Cr	H_3COH	*HCOO + H^+ + e^- → *HCOOH	1.35
	Fe	H_3COH	*HCOOH + H^+ + e^- → *H_2COOH	0.37
	Co	CH_4	*HCOOH + H^+ + e^- → *H_2COOH	0.39
	Nb	H_3COH	*OH + H^+ + e^-→ * + H_2O	1.09
	Ru	CH_4	*HCOOH + H^+ + e^- → *H_2COOH	0.46
	Rh	CH_4	*CO + H^+ + e^- → *HCO	1.06
	Pd	H_3COH	*HCOOH + H^+ + e^- → *HCO	0.33

	Ag	H_3COH	$*HCOOH + H^+ + e^- \rightarrow *HCO$	0.59
	Ir	CH_4	$*CO + H^+ + e^- \rightarrow *HCO$	1.12
	Pt	H_3COH	$*CO + H^+ + e^- \rightarrow *HCO$	0.69
	Au	H_3COH	$*HCOOH + H^+ + e^- \rightarrow *H_2COOH$	0.33
Ag-host	Sc	H_3COH	$*OH + H^+ + e^- \rightarrow * + H_2O$	0.85
	Ni	CH_4	$*HCOOH + H^+ + e^- \rightarrow *H_2COOH$	0.41
	Cu	H_3COH	$*HCOO + H^+ + e^- \rightarrow *HCOOH$	0.32
	Zr	H_3COH	$*OH + H^+ + e^- \rightarrow * + H_2O$	1.06
	Mo	H_3COH	$*O + H^+ + e^- \rightarrow *OH$	0.58
	Ru	CH_4	$*CO + H^+ + e^- \rightarrow *COH$	1.07
	Ta	H_3COH	$*OH + H^+ + e^- \rightarrow * + H_2O$	1.67
	W	H_3COH	$*OH + H^+ + e^- \rightarrow * + H_2O$	1.17
	Re	H_3COH	$*O + H^+ + e^- \rightarrow *OH$	0.80
	Ir	CH_4	$*CO + H^+ + e^- \rightarrow *HCO$	1.12
Ni-host	Pure	CH_4	$* + CO_2 \rightarrow *CO_2$	0.19
	V	H_3COH	$*OH + H^+ + e^- \rightarrow * + H_2O$	0.51
	Cr	CH_4	$*HCOO + H^+ + e^- \rightarrow *HCOOH$	0.21
	Zn	H_3COH	$*HCOOH + H^+ + e^- \rightarrow *H_2COOH$	0.26
	Y	CH_4	$*CO + H^+ + e^- \rightarrow *COH$	0.68
	Nb	H_3COH	$*OH + H^+ + e^- \rightarrow * + H_2O$	0.59
	Ag	CH_4	$* + CO_2 \rightarrow *CO_2$	0.16
	Hf	CH_4	$*COH + H^+ + e^- \rightarrow *C + H_2O$	0.28
	Os	CH_4	$*CO + H^+ + e^- \rightarrow *COH$	0.85
	Ir	CH_4	$*CO + H^+ + e^- \rightarrow *COH$	0.49
	Pt	CH_4	$*COH + H^+ + e^- \rightarrow *HCOH$	0.45
	Au	H_3COH	$*CO_2 + H^+ + e^- \rightarrow *HCOO$	0.16

Hydrogen evolution reaction (HER) is the major competing reaction for CO_2 reduction at low overpotential. Thus, it is necessary to compare HER vs. CO_2 reduction on the SAAs. All possible sites of the H atom adsorption on the different of SAAs (top, bridge, fcc and hcp) have been considered. The Gibbs free energies of HER (G_H) on above SAAs were calculated. The optimal structures and G_H on different sites are shown in Figure S75 and Table S5. The results of competitive comparison between HER and CO_2 reduction reaction are shown in Figure 1e. [48-50] As depicted, on ScCu,

FeCu, AuCu, CuAg and VNi SAAs, CO_2 reduction reactions are more likely to occur for target product CH_3OH. Notably, the corresponding G_{PDS} of these SAA catalysts, as by our calculation (ScCu, G_{PDS} = 0.24 eV; FeCu, G_{PDS} = 0.37 eV; AuCu, G_{PDS} = 0.33 eV; CuAg, G_{PDS} = 0.32 eV; VNi, G_{PDS} = 0.51 eV), are much lower than the other catalysts reported in previous literature,[51-53] which implies superior performance in electrochemical reduction of CO_2 into CH_3OH.

To improve the applicability of our DFT calculations to experimental conditions, the stability of these screened SAAs was evaluated by their aggregation energy (E_{agg}) and the segregation energy (E_{seg}). E_{agg} represents the thermodynamic stability of isolated dopant atoms compared to dopant clusters, while E_{seg} reflects the relative stability of isolated dopants in the surface layer of the host material compared to those in the bulk.[11] They are defined as follows: [15, 54]

$$E_{agg}(n) = E_{Tot}(n) + (n-1) * E_{Tot}(host) - n * E_{Tot}(SAA) \quad (4)$$

$$E_{seg} = E_{Tot}(bulk) - E_{Tot}(SAA) \quad (5)$$

where $E_{Tot}(n)$ and $E_{Tot}(host)$ are the DFT total energies of an alloy surface containing a cluster of n dopant atoms (with n = 2 considered) and the pure host material, respectively. $E_{Tot}(SAA)$ and $E_{Tot}(bulk)$ are the DFT total energies of the single guest atoms located in the surface layer and in the second layer of the host material slab, respectively. A negative E_{agg} value indicates a preference for surface clustering, whereas a positive E_{agg} value indicates a tendency for the dopant atom dispersion separately into the SAA structure. Similarly, a negative value of E_{seg} indicates that it is more energetically favorable for a single guest atom to reside in the bulk rather than at the

surface, which would render it catalytically inactive and unsuitable for practical applications. In contrast, a positive E_{seg} value indicates a preference for the guest atom to remain at the surface, which meets the requirements for catalytic activity. Thus, a stable SAA candidate should possess positive energies for both E_{agg} and E_{seg}.

The calculated E_{agg} and E_{seg} of the screened SAAs (ScCu, FeCu, AuCu, CuAg and VNi) are shown in Figure 2a and 2b, respectively. It can be seen that ScCu (E_{agg} of 0.93 eV and E_{seg} of 0.98 eV) and AuCu (E_{agg} of 0.20 eV and E_{seg} of 0.38 eV) show good stability in both aggregation and segregation perspectives. It is important to note that, to ensure sufficient data for ML training, all DFT calculated SAAs (477 elementary reactions) were utilized in the subsequent section, rather than limiting the dataset to only the G_{PDS} and stability screened SAAs.

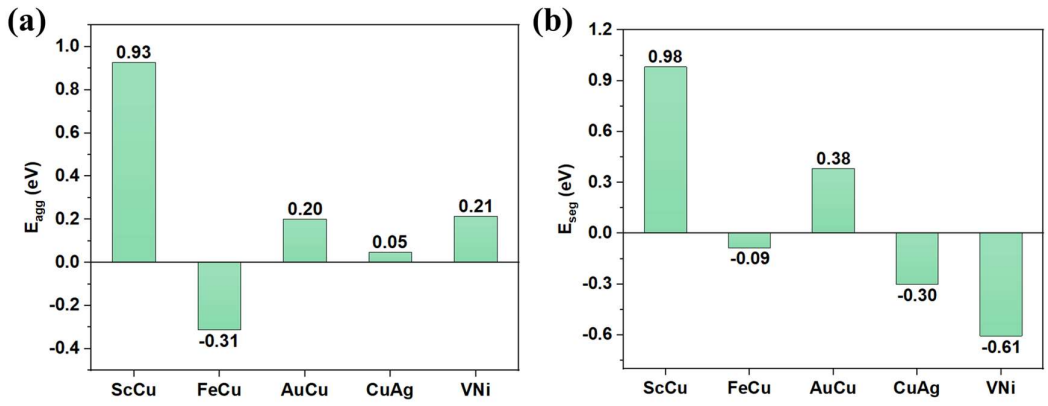

Figure 2. (a) E_{agg} and (b) E_{seg} of the DFT screened SAAs favoring CH_3OH production.

Machine learning. Previous studies have demonstrated the efficacy of utilizing the physicochemical properties in prediction.[28, 39] In our case, the atomic number of guest atom and host atom (Z_g and Z_h), the radius of guest atom and host atom (R_g and R_h), the period of guest atom and host atom (P_g and P_h), the number of

peripheral electrons of guest atom and host atom (N_g and N_h), the relative atomic mass of guest atom and host atom (M_g and M_h), the first ionization energy of guest atom and host atom (Ei_g and Ei_h), the electronegativity of guest atom and host atom (X_g and X_h), the electron affinity of guest atom and host atom (EA_g and EA_h), were included, as shown in Table S5. To describe the Gibbs free energy of CO_2 reduction reaction, five parameters were selected, namely, the sum of relative molecular masses of reactants and products (SM), the sum of the number of C-H bonds of reactants and products (SN), the sum of energies of reactants and products (SE), the sum of the number of H atoms of reactants and products (SNH), and the sum of the number of O atoms of reactants and products (SNO), as shown in Table S6 and S7. All these parameters, 21 features in total, were selected as candidates for the feature set.

Creating an optimal feature set is essential for building a ML model with high precision. Balancing the selection of features is crucial because too many features can lead to redundancy, while too few features may not meet the basic requirements for model establishment. Consequently, we conducted Pearson correlation analysis to investigate the interrelationships among the initial 21 features, as shown in Figure S76. It is evident that numerous features exhibit high correlation, and an excessive number of such attributes could potentially exacerbate the "curse of dimensionality", thereby increasing susceptibility to overfitting.[55] To obtain the optimal features, the feature recursive elimination (FRE) method was employed to refine the initial feature set. The FRE score serves as a metric to gauge the effectiveness of a feature in describing the target value, with higher scores indicating a stronger correlation between the feature

and the target. As shown in Figure 3a, the FRE score shows the maximum when the number of features is seven, indicating the optimal subset of features for the given analysis. The suggested features include R_g, N_g, M_g, M_h, SM, SN and SE. Their Pearson correlation analysis is shown in Figure 3b, which exhibits low correlations, suggesting that the selected seven features are both reasonable and indispensable for the analysis at hand. It is noted that SM and SE exhibit higher Pearson correlation. SE is a complementary feature of different elementary reactions by SM, because some elementary reactions (for example, $*CO_2 + H^+ + e^- \rightarrow *COOH$ and $*CO_2 + H^+ + e^- \rightarrow *HCOO$) have the same SM but different SE (Table S7), which can help us better distinguish different elementary reactions. Figure 3c also proves that they are indispensable. To understand the relationship between the features and the targeted property (Gibbs free energies of elementary reactions), the importance of the seven selected features was evaluated, the results are shown in Figure 3c. From the results, one can see that the SM, SE and R_g emerge as the most influential factors in determining the Gibbs free energy, contributing 29.39%, 24.05% and 13.52% respectively. These three features' value collectively account for more than 60%, suggesting that the type of elementary reaction and the guest atoms of SAAs play a dominant role in determining the Gibbs free energy. This deduction is consistent with the properties observed in previously studied SAAs.[43, 56, 57] The remaining factors account for values ranging from 6.88% to 9.87%. The similar degree of importance observed among the evaluated features further reinforces the validity of our feature selection process. Hence, the combination of these seven features along with the dataset

of 477 Gibbs free energies for CO_2 reduction on SAAs will be employed to construct a robust ML model.

The precision of ML prediction relies heavily on the choice of algorithm. Even experienced data scientists cannot definitively determine which algorithm performs best without experimenting with various options. Therefore, in this work, 6 different ML models were evaluated by using the preprocessed dataset, including Linear, Ridge, Lasso, BRR, GBR and KNR. The dataset was randomly divided into a training set (80%) and a test set (20%) to ensure the generalization and accuracy of the ML model. This divided ratio is commonly regarded as optimal for most algorithms. [4, 28, 58] The detailed parameters of all models can be found in Table S8.

The average RMSE and R^2 score for the 6 ML models after 500 repeated trainings are shown in Figure 3d and Figure S77. The GBR and KNR models show the best performance with the highest R^2 (0.99 for GBR model and 0.95 for KNR model) and the lowest RMSE (0.06 eV for GBR model and 0.13 eV for KNR model) in both training and test sets, as shown in Figure 3d. The highly consistent prediction errors observed in both the training set and test set indicate that the two models possess strong generalization ability. The other models (BRR, Lasso, Linear and Ridge) have unsatisfactory prediction performances because of high RMSE values and low R^2 score, as shown in Figure S77.

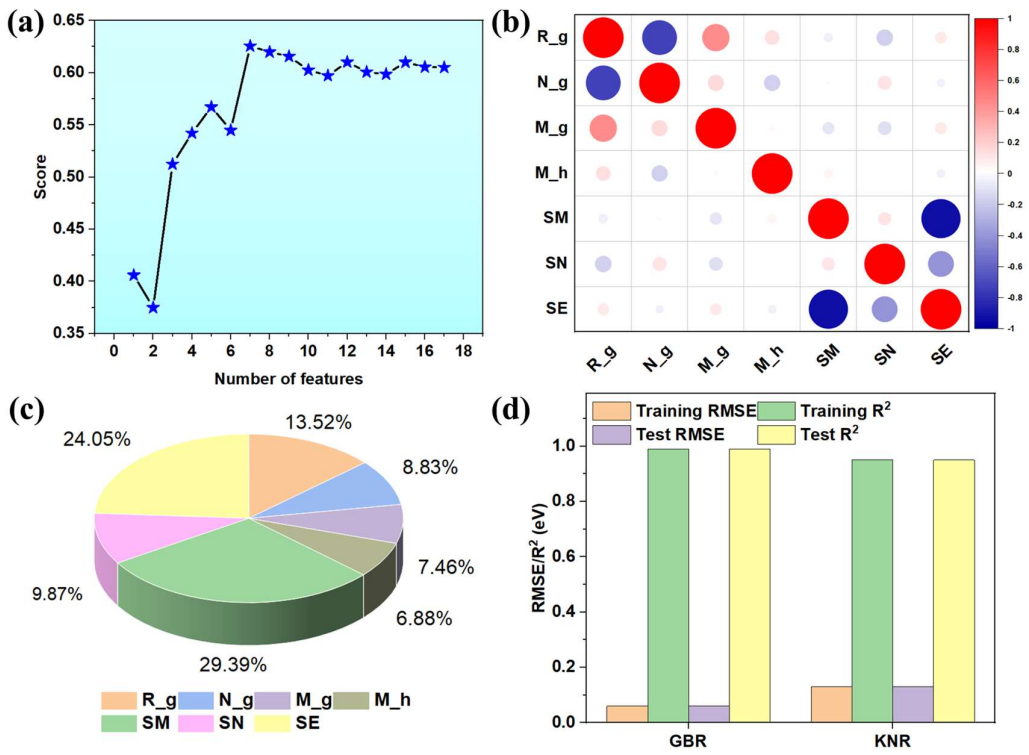

Figure 3. (a) Relationship between the number of features and the score of the model in the RFE method. (b) Pearson correlation map between the seven input features. (c) Feature importance for the reaction on different SAAs. (d) Distribution of the R^2 score and RMSE for the GBR and KNR models in 500 repeated trials.

After the model training and testing procedure, the best-performing GBR and KNR models were further applied to predict the Gibbs free energies of elementary reactions for electrochemical CO_2 reduction of another 46 unknown SAA catalysts, including Ti-, V-, Mn-, Ni-, Zn-, Y-, Zr-, Mo-, Cd-, Hf-, Ta-, W-, Re-, and Os-doped in Cu-host SAAs, Ti-, V-, Cr-, Mn-, Fe-, Co-, Zn-, Y-, Nb-, Rh-, Pd-, Cd-, Hf-, Os-, Pt-, and Au-doped in Ag-host SAAs, Sc-, Ti-, Mn-, Fe-, Co-, Cu-, Zr-, Mo-, Ru-, Rh-, Pd-, Cd-, Ta-, W-, and Re-doped in Ni-host SAAs, and pure Ag metal. The input set data are

shown in Table S5 and S7. In total, 1610 Gibbs free energies of elementary reactions on the unknown 46 SAAs were predicted. Based on Scheme 1, we summarized the reaction pathways of CO_2 reduction to CH_4 or CH_3OH predicted by the GBR and KNR models in Table S9-S11. Note that the results of ML model predictions in Tables S9-S11 are the averages of the prediction values obtained through 5 repeated training sessions. It can be seen that some Gibbs free energies predicted the KNR model are not displayed in the tables because the KNR model does not differentiate the Gibbs free energies of different partial elementary reactions. For instance, the predicted Gibbs free energy values for two different elementary reactions of YCu, $*CO + H^+ + e^- \rightarrow *COH$ and $*CO + H^+ + e^- \rightarrow *HCO$, are both 0.66 eV. In addition, for the same reaction involving two different SAAs, such as HfCu and TaCu, the KNR model provides the same predicted values. These results suggest that the KNR model might not be able to effectively distinguish between different reaction routes and catalysts in the ML predictions. In addition, KNR model is considered a lazy learning algorithm as it does not actively learn from the training data, but rather memorizes it and uses this data to classify new input. [59] On the other hand, the GBR model has demonstrated remarkable fitting performance in previous literature. [6, 28, 60, 61] Similarly, in our case, the GBR model outperforms the KNR model in both R^2 and RMSE. Hence, only GBR model was chosen in the subsequent analyses.

Figure 4 and Table 2 summarized the predicted results of products, PDS and G_{PDS} on these unknown SAAs by GBR model. Based on the predicted results, it is apparent that Cu- and Ag-host SAAs are more inclined to produce CH_3OH, whereas Ni-host

SAAs are more prone to produce CH_4, which aligns well with our DFT calculations.

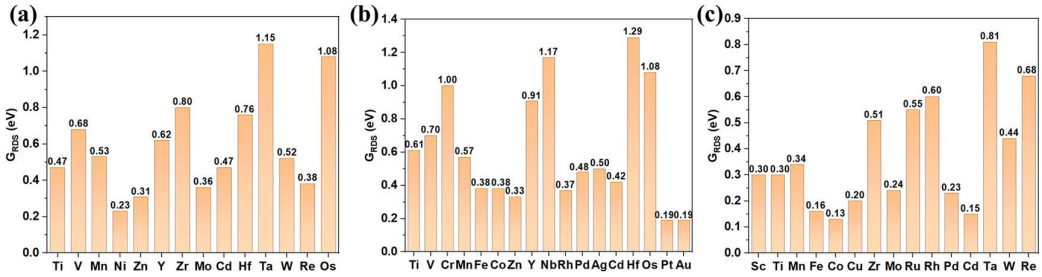

Figure 4. The prediction results of G_{PDS} on (a) Cu-, (b) Ag- and (c) Ni-host SAAs.

Table 2. The prediction results of product, PDS, and G_{PDS} on different SAAs for CO_2 reduction by GBR model.

SAA		Product	PDS	G_{PDS} (eV)
Cu-host	Ti	H_3COH	$*HCOO + H^+ + e^- \rightarrow *HCOOH$	0.47
	V	H_3COH	$*HCOO + H^+ + e^- \rightarrow *HCOOH$	0.68
	Mn	H_3COH	$*HCOO + H^+ + e^- \rightarrow *HCOOH$	0.53
	Ni	CH_4	$*HCOO + H^+ + e^- \rightarrow *HCOOH$ $*HCOOH + H^+ + e^- \rightarrow *HCO + H_2O$	0.23
	Zn	H_3COH	$*HCOOH + H^+ + e^- \rightarrow *H_2COOH$	0.31
	Y	H_3COH	$*OH + H^+ + e^- \rightarrow * + H_2O$	0.62
	Zr	H_3COH	$*OH + H^+ + e^- \rightarrow * + H_2O$	0.80
	Mo	H_3COH	$*HCOO + H^+ + e^- \rightarrow *HCOOH$	0.36
	Cd	H_3COH	$*HCOOH + H^+ + e^- \rightarrow *H_2COOH$	0.47
	Hf	H_3COH	$*OH + H^+ + e^- \rightarrow * + H_2O$	0.76
	Ta	H_3COH	$*OH + H^+ + e^- \rightarrow * + H_2O$	1.15
	W	H_3COH	$*OH + H^+ + e^- \rightarrow * + H_2O$	0.52
	Re	H_3COH	$*HCOO + H^+ + e^- \rightarrow *HCOOH$	0.38
	Os	CH_4	$*CO + H^+ + e^- \rightarrow *HCO$	1.08
Ag-host	Pure	H_3COH	$*HCOOH + H^+ + e^- \rightarrow *HCO$	0.50
	Ti	H_3COH	$*OH + H^+ + e^- \rightarrow * + H_2O$	0.61
	V	H_3COH	$*HCOO + H^+ + e^- \rightarrow *HCOOH$	0.70
	Cr	H_3COH	$*HCOO + H^+ + e^- \rightarrow *HCOOH$	1.00
	Mn	CH_4	$*HCOO + H^+ + e^- \rightarrow *HCOOH$	0.57
	Fe	CH_4	$*HCOO + H^+ + e^- \rightarrow *HCOOH$	0.38
	Co	CH_4	$*HCOOH + H^+ + e^- \rightarrow *H_2COOH$	0.38
	Zn	H_3COH	$*HCOOH + H^+ + e^- \rightarrow *H_2COOH$	0.33
	Y	H_3COH	$*OH + H^+ + e^- \rightarrow * + H_2O$	0.91

	Nb	H_3COH	$*OH + H^+ + e^- \rightarrow * + H_2O$	1.17
	Rh	CH_4	$*HCOOH + H^+ + e^- \rightarrow *H_2COOH$	0.37
	Pd	H_3COH	$*HCOOH + H^+ + e^- \rightarrow *H_2COOH$	0.48
	Cd	H_3COH	$*HCOOH + H^+ + e^- \rightarrow *H_2COOH$	0.42
	Hf	H_3COH	$*OH + H^+ + e^- \rightarrow * + H_2O$	1.29
	Os	CH_4	$*CO + H^+ + e^- \rightarrow *HCO$	1.08
	Pt	H_3COH	$*HCOOH + H^+ + e^- \rightarrow *H_2COOH$	0.19
	Au	H_3COH	$*HCOOH + H^+ + e^- \rightarrow *H_2COOH$	0.19
Ni-host	Sc	H_3COH	$*OH + H^+ + e^- \rightarrow * + H_2O$	0.30
	Ti	H_3COH	$*HCOO + H^+ + e^- \rightarrow *HCOOH$ $*OH + H^+ + e^- \rightarrow * + H_2O$	0.30
	Mn	CH_4	$*HCOO + H^+ + e^- \rightarrow *HCOOH$	0.34
	Fe	CH_4	$*HCOO + H^+ + e^- \rightarrow *HCOOH$	0.16
	Co	CH_4	$*HCOOH + H^+ + e^- \rightarrow *HCO + H_2O$	0.13
	Cu	CH_4	$*HCOOH + H^+ + e^- \rightarrow *H_2COOH$	0.20
	Zr	H_3COH	$*OH + H^+ + e^- \rightarrow * + H_2O$	0.51
	Mo	H_3COH	$*HCOO + H^+ + e^- \rightarrow *HCOOH$	0.24
	Ru	CH_4	$*CO + H^+ + e^- \rightarrow *COH$	0.55
	Rh	CH_4	$*CO + H^+ + e^- \rightarrow *COH$	0.60
	Pd	CH_4	$*HCOOH + H^+ + e^- \rightarrow *HCO$	0.23
	Cd	H_3COH	$*HCOOH + H^+ + e^- \rightarrow *H_2COOH$	0.15
	Ta	H_3COH	$*OH + H^+ + e^- \rightarrow * + H_2O$	0.81
	W	CH_4	$*CO + H^+ + e^- \rightarrow *COH$	0.44
	Re	CH_4	$*CO + H^+ + e^- \rightarrow *COH$	0.68

To verify the predicted potential SAA catalysts for electrochemical CO_2 reduction to CH_3OH, three predicted SAAs were further investigated using DFT calculations, including ZnCu, AuAg and MoNi, which exhibit the lowest G_{PDS} among Cu-, Ag- and Ni-host SAAs, respectively. It should be noted that although CdNi has the lowest G_{PDS} among the Ni-host SAA, the Cd atoms protrude on the Ni surface, causing its structure to differ from other SAAs (Figure S78), and thus the second lowest MoNi was selected for verification. Figure 5 shows the results of Gibbs free energies of elementary reactions by GBR predictions (G_{GBR}) and DFT calculations (G_{DFT}). Although CO_2

undergoes different reaction pathways to produce CH_3OH on the three SAAs (Table S9-S11), they all involve a 6-step reduction process:

$$CO_2 + 6H^+ + 6e^- \rightarrow CH_3OH + H_2O \quad (6)$$

Hence, steps 1-7 were used here to represent the CO_2 adsorption and electrochemical reduction process. The results indicate that the GBR model shows good predictive capabilities. About 50% of the difference between G_{GBR} and G_{DFT} is less than 0.1 eV, and more than 75% is less than 0.3 eV. For AuAg, the differences between G_{GBR} and G_{DFT} of steps 4, 5 and 7 are more than 0.4 eV. The underlying reason may be that the adsorbed intermediate species $*H_2COOH$ and $*CH_3O$ are no longer adsorbed on the guest atom (Au atom) but on the host atom (Ag atom) next to the guest atom (Figure S80). The optimal structures of the three SAAs are shown in Figure S79-81.

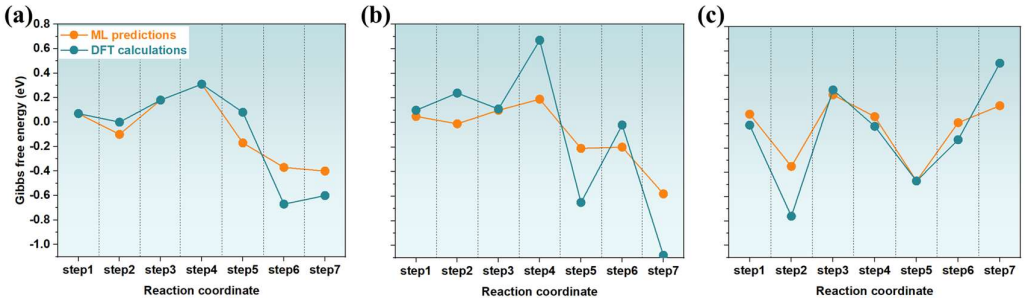

Figure 5. The results of Gibbs free energies of GBR model predicts and DFT calculations, (a) ZnCu, (b) AuAg and (c) MoNi.

After DFT verification, the SAAs predicted by ML were screened. According to the previous screening criteria (the product is CH_3OH and $G_{PDS} < 0.68$ eV), the predicted results suggest that TiCu ($G_{PDS} = 0.47$ eV), MnCu ($G_{PDS} = 0.53$ eV), ZnCu ($G_{PDS} = 0.31$ eV), YCu ($G_{PDS} = 0.62$ eV), MoCu ($G_{PDS} = 0.36$ eV), CdCu ($G_{PDS} = 0.47$

eV), WCu (G_{PDS} = 0.52 eV), ReCu (G_{PDS} = 0.38 eV), TiAg (G_{PDS} = 0.61 eV), ZnAg (G_{PDS} = 0.33 eV), PdAg (G_{PDS} = 0.48 eV), CdAg (G_{PDS} = 0.42 eV), PtAg (G_{PDS} = 0.19 eV), AuAg (G_{PDS} = 0.19 eV), ScNi (G_{PDS} = 0.30 eV), TiNi (G_{PDS} = 0.30 eV), ZrNi (G_{PDS} = 0.51 eV), MoNi (G_{PDS} = 0.24 eV), CdNi (G_{PDS} = 0.15 eV), and pure Ag metal (G_{PDS} = 0.50 eV) are promising catalysts for CO_2 reduction to CH_3OH.

To ensure that these 20 SAAs catalysts screened are indeed favor the production of CH_3OH, additional analysis and refinement were conducted. The possible reaction pathways leading to the formation of CH_3OH and the by-product CH_4 for these 20 SAAs screened are summarized in Table S12. For instance, in some of these SAAs, the primary distinctive step for CH_3OH and CH_4 lies in the subsequent reaction of the $*H_2COOH$ intermediate. If $*H_2COOH$ generates $*H_2CO$ and H_2O, the route afterwards might favor CH_4 production. Yet $*H_2COOH$ may also generate *O and CH_3OH. The energies of such competitive reactions might be close. To eliminate such influence for the prediction, more stringent criteria should be established. Thus, an additional criterion was proposed: the value of energy difference between the key branching competitive reaction for CH_3OH and CH_4 formation must be higher than 0.33 eV, which is the average value of the energy difference for the key competitive reactions in these 20 SAAs screened, and is sufficiently large to indicate that the reaction on the selected SAAs truly favors CH_3OH formation over CH_4. The screened SAAs that favor CH_3OH production include TiCu, YCu, MoCu, WCu, ReCu, TiAg, ScNi and MoNi. Finally, the stability of these ML-predicted SAAs was evaluated accordingly (Figure 6a and 6b). Among them, YCu (E_{agg} = 1.48 eV and E_{seg} = 2.83 eV) and ScNi (E_{agg} = 0.77 eV and

E_{seg} = 1.34 eV) exhibit high stability against aggregation and segregation, indicating their promising potential as effective catalysts for CO_2 reduction into CH_3OH.

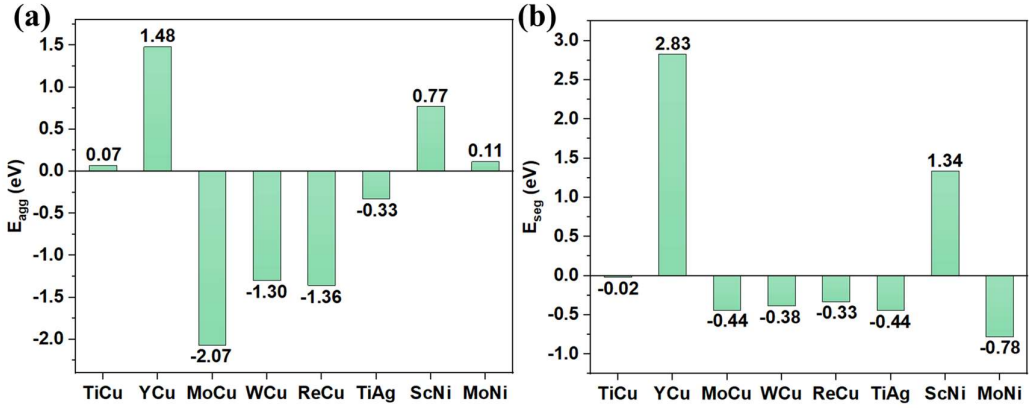

Figure 6. (a) E_{agg} and (b) E_{seg} of the ML predicted SAAs favoring CH_3OH production.

Conclusions

In summary, we have systematically performed DFT and ML studies to investigate the CO_2 electrochemical reduction to CH_3OH on all possible Cu-, Ag- and Ni-host SAAs. A total of 477 Gibbs free energies of elementary reactions on 35 SAAs from DFT calculations were utilized to train the ML model, which were then applied to predict the Gibbs free energies of 1610 elementary reactions on 46 unknown SAAs to determine their pathways, products, PDS and G_{PDS}. Six different ML models were trained and among which, the GBR model exhibited the best performance, achieving a RMSE of 0.06 eV and an R^2 score of 0.99. It was then extended to predict the Gibbs free energies of unknown SAAs for the CO_2 electrochemical reduction. The Gibbs free energies of ML predictions were verified by DFT calculations with high accuracy (half of their lower than 0.1 eV). Based on our DFT calculations and ML predictions, after careful energetic screening and stability evaluation, it is suggested that ScCu, YCu, AuCu and ScNi may be the promising SAA catalysts for CO_2 reduction into CH_3OH.

In general, the ML-assisted approach offers direct and reliable guidance for predicting Gibbs free energies with significantly lower computational cost. This efficient screening method is expected to greatly enhance the rational design of new catalysts for CO_2 reduction to CH_3OH. Future research in this area warrants further attention.

Conflicts of interest

There are no conflicts to declare.

Data availability and reproducibility statement

The numerical data from Figures 1 and 5 and Table 1 are tabulated in the Supporting Information (Figures S2-S75, Tables S3 and S4). The numerical data from Figures 2 and 6 come from the energy calculations after structural optimization based on equations 4 and 5, the relevant structures are tabulated in opt_SAA.zip. The numerical data from Figures 3-5 and Table 2 are tabulated in the Supporting Information (Figures S76-S77, Figures S79-S81, Tables S9-S11). All the DFT data were obtained using VASP, with the computational details provided in Methods section of manuscript and Computational Details section of the Supporting Information. The optimized configurations of SAAs are tabulated in opt_SAA.zip, the optimized configurations after SAAs adsorption are tabulated in the Supporting Information (Figures S2-S75, Figures S78-81). The ML data were generated using the open-source Scikit-learn package in the Python3 environment. The ML input data are tabulated in the Supporting Information (Tables S5-S8) and in training_data.xlsx. The ML output data are tabulated in the Supporting Information (Tables S9-S11) and in prediction_data.xlsx.

Acknowledgments

This work was supported by the National Natural Science Foundation of China (No. 22202024, 22108019, 22108018), the Chongqing Science and Technology Commission (No. CSTB2022NSCQ-BHX0021), the China Scholarship Council (No. 202206050117), the Italy-Singapore Science and Technology Cooperation (Grant No. R22I0IR121), and the Singapore A*STAR SERC CRF Award. The use of computing resources at the A*STAR Computational Resource Centre (A*CRC) and National Supercomputer Centre, Singapore (NSCC) is gratefully acknowledged. The authors thank to Yuan Ye for the code support.

References

1. Masson-Delmotte, V.; Zhai, P.; Pörtner, H.-O.; Roberts, D.; Skea, J.; Shukla, P. R., *Global Warming of 1.5 C: IPCC special report on impacts of global warming of 1.5 C above pre-industrial levels in context of strengthening response to climate change, sustainable development, and efforts to eradicate poverty*. Cambridge University Press: 2022.
2. Hu, E.; Liu, C.; Zhang, W.; Yan, Q., Machine Learning Assisted Understanding and Discovery of CO_2 Reduction Reaction Electrocatalyst. *J. Phys. Chem. C* **2023,** *127*, 882-893.
3. Ma, M.; Tang, Q., Axial Coordination Modification of M–N_4 Single-Atom Catalysts to Regulate the Electrocatalytic CO_2 Reduction Reaction. *J. Mater. Chem. C* **2022,** *10*, 15948-15956.
4. Yılmaz, B.; Oral, B.; Yıldırım, R., Machine Learning Analysis of Catalytic CO_2

Methanation. *Int. J. Hydrogen Energ.* **2023,** *48*, 24904-24914.

5. Khoo, H. H.; Halim, I.; Handoko, A. D., LCA of Electrochemical Reduction of CO_2 to Ethylene. *J. CO_2 Util.* **2020,** *41*, 101229.
6. Yu, L.; Li, F.; Huang, J.; Sumpter, B. G.; Mustain, W. E.; Chen, Z., Double-Atom Catalysts Featuring Inverse Sandwich Structure for CO_2 Reduction Reaction: A Synergetic First-Principles and Machine Learning Investigation. *ACS Catal.* **2023,** *13*, 9616-9628.
7. Qin, L.; Sun, F.; Ma, X.; Ma, G.; Tang, Y.; Wang, L.; Tang, Q.; Jin, R.; Tang, Z., Homoleptic Alkynyl-Protected Ag_{15} Nanocluster with Atomic Precision: Structural Analysis and Electrocatalytic Performance toward CO_2 Reduction. *Angew. Chem. Int. Ed.* **2021,** *60*, 26136-26141.
8. Hori, Y.; Wakebe, H.; Tsukamoto, T.; Koga, O., Adsorption of CO Accompanied with Simultaneous Charge Transfer on Copper Single Crystal Electrodes Related with Electrochemical Reduction of CO_2 to Hydrocarbons. *Surf. Sci.* **1995,** *335*, 258-263.
9. Luo, S.; Zhang, L.; Liao, Y.; Li, L.; Yang, Q.; Wu, X.; Wu, X.; He, D.; He, C.; Chen, W.; Wu, Q.; Li, M.; Hensen, E. J. M.; Quan, Z., A Tensile-Strained Pt–Rh Single-Atom Alloy Remarkably Boosts Ethanol Oxidation. *Adv. Mater.* **2021,** *33*, 2008508.
10. Marcinkowski, M. D.; Darby, M. T.; Liu, J.; Wimble, J. M.; Lucci, F. R.; Lee, S.; Michaelides, A.; Flytzani-Stephanopoulos, M.; Stamatakis, M.; Sykes, E. C. H., Pt/Cu Single-Atom Alloys as Coke-Resistant Catalysts for

Efficient C–H Activation. *Nat. Chem.* **2018,** *10*, 325-332.

11. Hannagan, R. T.; Giannakakis, G.; Flytzani-Stephanopoulos, M.; Sykes, E. C. H., Single-Atom Alloy Catalysis. *Chem. Rev.* **2020,** *120*, 12044-12088.
12. Jiang, J.-C.; Chen, J.-C.; Zhao, M.-d.; Yu, Q.; Wang, Y.-G.; Li, J., Rational Design of Copper-Based Single-Atom Alloy Catalysts for Electrochemical CO_2 Reduction. *Nano Res.* **2022,** *15*, 7116-7123.
13. Cheng, M.-J.; Clark, E. L.; Pham, H. H.; Bell, A. T.; Head-Gordon, M., Quantum Mechanical Screening of Single-Atom Bimetallic Alloys for the Selective Reduction of CO_2 to C_1 Hydrocarbons. *ACS Catal.* **2016,** *6*, 7769-7777.
14. Xie, H.; Wan, Y.; Wang, X.; Liang, J.; Lu, G.; Wang, T.; Chai, G.; Adli, N. M.; Priest, C.; Huang, Y.; Wu, G.; Li, Q., Boosting Pd-catalysis for Electrochemical CO_2 RAeduction to CO on Bi-Pd Single Atom Alloy Nanodendrites. *Appl. Catal. B: Environ.* **2021,** *289*, 119783.
15. Zhou, W.; Chen, Y.; Tan, L.; Tang, Q.; Lu, C.; Dong, L., Understanding the C-H Activation of Methane over Single-Atom Alloy Catalysts by Density Functional Theory Calculations. *AIChE J.* **2023,** *69*, e18118.
16. Shan, J.; Liu, J.; Li, M.; Lustig, S.; Lee, S.; Flytzani-Stephanopoulos, M., NiCu Single Atom Alloys Catalyze the C-H Bond Activation in the Selective Non-Oxidative Ethanol Dehydrogenation Reaction. *Appl. Catal. B: Environ.* **2018,** *226*, 534-543.
17. Zheng, T.; Liu, C.; Guo, C.; Zhang, M.; Li, X.; Jiang, Q.; Xue, W.; Li, H.; Li, A.; Pao, C.-W.; Xiao, J.; Xia, C.; Zeng, J., Copper-Catalysed

Exclusive CO_2 to Pure Formic Acid Conversion via Single-Atom Alloying. *Nat. Nanotechnol.* **2021,** *16*, 1386-1393.

18. Cao, Y.; Chen, S.; Bo, S.; Fan, W.; Li, J.; Jia, C.; Zhou, Z.; Liu, Q.; Zheng, L.; Zhang, F., Single Atom Bi Decorated Copper Alloy Enables C−C Coupling for Electrocatalytic Reduction of CO_2 into C_{2+} Products. *Angew. Chem. Int. Ed.* **2023,** *62*, e202303048.
19. Zhang, Z.-Y.; Wang, H.-B.; Zhang, F.-F.; Li, J.-W.; Hu, X.-Z.; Yan, S.-W.; Bai, Y.-M.; Zhang, X.; Shen, G.-R.; Yin, P.-F.; Yang, J.; Dong, C.-K.; Mao, J.; Liu, H.; Du, X.-W., Nanocavity Enriched CuPd Alloy with High Selectivity for CO_2 Electroreduction toward C_2H_4. *Rare Met.* **2024,** *43*, 1513-1523.
20. Neto, M. M. C. B.; Verga, L. G.; Da Silva, J. L. F.; Galvão, B. R. L., Computational Screening of Silver-Based Single-Atom Alloys Catalysts for CO_2 Reduction. *J. Chem. Phys.* **2024,** *160*.
21. Chen, A.; Zhang, X.; Chen, L.; Yao, S.; Zhou, Z., A Machine Learning Model on Simple Features for CO_2 Reduction Electrocatalysts. *J. Phys. Chem. C* **2020,** *124*, 22471-22478.
22. Rittiruam, M.; Khamloet, P.; Ektarawong, A.; Atthapak, C.; Saelee, T.; Khajondetchairit, P.; Alling, B.; Praserthdam, S.; Praserthdam, P., Screening of Cu-Mn-Ni-Zn High-Entropy Alloy Catalysts for CO2 Reduction Reaction by Machine-Learning-Accelerated Density Functional Theory. *Appl. Surf. Sci.* **2024,** *652*, 159297.
23. Roy, D.; Mandal, S. C.; Pathak, B., Machine Learning-Driven High-Throughput

Screening of Alloy-Based Catalysts for Selective CO_2 Hydrogenation to Methanol. *ACS Appl. Mater. Interfaces* **2021,** *13*, 56151-56163.

24. Kresse, G.; Furthmuller, J., Efficiency of Ab-initio Total Energy Calculations for Metals and Semiconductors Using a Plane-Wave Basis Set. *Comput. Mater. Sci* **1996,** *6*, 15-50.
25. Kresse, G.; Furthmüller, J., Efficient Iterative Schemes for Ab Initio Total-Energy Calculations Using a Plane-Wave Basis Set. *Phys. Rev. B* **1996,** *54*, 11169-11186.
26. Kresse, G.; Hafner, J., Ab Initio Molecular Dynamics for Open-Shell Transition Metals. *Phys. Rev. B* **1993,** *48*, 13115-13118.
27. Abild-Pedersen, F.; Greeley, J.; Studt, F.; Rossmeisl, J.; Munter, T. R.; Moses, P. G.; Skúlason, E.; Bligaard, T.; Nørskov, J. K., Scaling Properties of Adsorption Energies for Hydrogen-Containing Molecules on Transition-Metal Surfaces. *Phys. Rev. Lett.* **2007,** *99*, 016105.
28. Feng, H.; Ding, H.; Wang, S.; Liang, Y.; Deng, Y.; Yang, Y.; Wei, M.; Zhang, X., Machine-Learning-Assisted Catalytic Performance Predictions of Single-Atom Alloys for Acetylene Semihydrogenation. *ACS Appl. Mater. Interfaces* **2022,** *14*, 25288-25296.
29. Barone, V. T.; Tuttle, B. R.; Khare, S. V., Properties of $AgBiI_4$ using High Through-Put DFT and Machine Learning Methods. *J. Appl. Phys.* **2022,** *131*, 245701.
30. Back, S.; Tran, K.; Ulissi, Z. W., Toward a Design of Active Oxygen Evolution Catalysts: Insights from Automated Density Functional Theory Calculations and

Machine Learning. *ACS Catal.* **2019,** *9*, 7651-7659.

31. Grimme, S., Semiempirical GGA-type density functional constructed with a long-range dispersion correction. *J. Comput. Chem.* **2006,** *27*, 1787-1799.
32. Zhang, Y.; Li, S.; Sun, C.; Wang, P.; Yang, Y.; Yi, D.; Wang, X.; Yao, J., Understanding and Modifying the Scaling Relations for Ammonia Synthesis on Dilute Metal Alloys: From Single-Atom Alloys to Dimer Alloys. *ACS Catal.* **2022,** *12*, 9201-9212.
33. Sun, S.; Sun, G.; Pei, C.; Zhao, Z.-J.; Gong, J., Origin of Performances of Pt/Cu Single-Atom Alloy Catalysts for Propane Dehydrogenation. *J. Phys. Chem. C* **2021,** *125*, 18708-18716.
34. Mohan, O.; Xu, R.; Mushrif, S. H., Novel Nickel-Based Single-Atom Alloy Catalyst for CO_2 Conversion Reactions: Computational Screening and Reaction Mechanism Analysis. *J. Phys Chem. C* **2021,** *125*, 4041-4055.
35. Chen, Y.; Sun, F.; Tang, Q., Computational Insights and Design of Promising Ultrathin PdM Bimetallenes for Oxygen Reduction Electrocatalysis. *Small Methods* **2023,** *7*, 2300276.
36. Nørskov, J. K.; Rossmeisl, J.; Logadottir, A.; Lindqvist, L.; Kitchin, J. R.; Bligaard, T.; Jónsson, H., Origin of the Overpotential for Oxygen Reduction at a Fuel-Cell Cathode. *J. Phys. Chem. B* **2004,** *108*, 17886-17892.
37. Ma, M.; Li, F.; Tang, Q., Coordination Environment Engineering on Nickel Single-Atom Catalysts for CO_2 Electroreduction. *Nanoscale* **2021,** *13*, 19133-19143.

38. Pedregosa, F.; Varoquaux, G.; Gramfort, A.; Michel, V.; Thirion, B.; Grisel, O.; Blondel, M.; Prettenhofer, P.; Weiss, R.; Dubourg, V., Scikit-Learn: Machine Learning in Python. *J. Mach. Learn. Res.* **2011,** *12*, 2825-2830.

39. Feng, H.; Zhang, M.; Ge, Z.; Deng, Y.; Pu, P.; Zhou, W.; Yuan, H.; Yang, J.; Li, F.; Zhang, X.; Zhang, Y.-W., Designing Efficient Single-Atom Alloy Catalysts for Selective C═O Hydrogenation: A First-Principles, Active Learning and Microkinetic Study. *ACS Appl. Mater. Interfaces* **2023,** *15*, 55903-55915.

40. Giannakakis, G.; Flytzani-Stephanopoulos, M.; Sykes, E. C. H., Single-Atom Alloys as a Reductionist Approach to the Rational Design of Heterogeneous Catalysts. *Acc. Chem. Res.* **2019,** *52*, 237-247.

41. Yin, J.; Ehara, M.; Sakaki, S., Single Atom Alloys vs. Phase Separated Alloys in Cu, Ag, and Au Atoms with Ni(111) and Ni, Pd, and Pt Atoms with Cu(111): a Theoretical Exploration. *Phys. Chem. Chem. Phys.* **2022,** *24*, 10420-10438.

42. Liu, W.; Feng, H.; Yang, Y.; Niu, Y.; Wang, L.; Yin, P.; Hong, S.; Zhang, B.; Zhang, X.; Wei, M., Highly-Efficient RuNi Single-Atom Alloy Catalysts toward Chemoselective Hydrogenation of Nitroarenes. *Nat. Commun.* **2022,** *13*, 3188.

43. Shen, T.; Wang, S.; Zhao, T.; Hu, Y.; Wang, D., Recent Advances of Single-Atom-Alloy for Energy Electrocatalysis. *Adv. Energy Mater.* **2022,** *12*, 2201823.

44. Schumann, J.; Bao, Y.; Hannagan, R. T.; Sykes, E. C. H.; Stamatakis, M.; Michaelides, A., Periodic Trends in Adsorption Energies around Single-Atom

Alloy Active Sites. *J. Phys. Chem. Lett.* **2021,** *12*, 10060-10067.

45. Zhu, Q.; Gu, Y.; Wang, X.; Gu, Y.; Ma, J., The Synergistic Effect between Metal and Sulfur Vacancy to Boost CO_2 Reduction Efficiency: A Study on Descriptor Transferability and Activity Prediction. *JACS Au* **2024,** *4*, 125-138.
46. Xiong, B.; Yang, Y.; Liu, J.; Hua, Z.; Yang, Y., Electrocatalytic Reduction of CO_2 to C_1 Products over Bimetal Catalysts: A DFT Screening Study. *Fuel Process. Technol.* **2022,** *233*, 107315.
47. Yang, Y.; Wang, J.; Shu, Y.; Ji, Y.; Dong, H.; Li, Y., Significance of Density Functional Theory (DFT) Calculations for Electrocatalysis of N_2 and CO_2 Reduction Reactions. *Phys. Chem. Chem. Phys.* **2022,** *24*, 8591-8603.
48. Wang, J.; Zhao, K.; Yi, D.; Yang, Y.; Wang, X., Role of Single-Atom Alloy Catalysts in Electrochemical Conversion of Carbon Dioxide: A Theoretical Study. *Chem. Eng. Sci.* **2024,** *290*, 119910.
49. Qi, R.; Zhu, B.; Han, Z.; Gao, Y., High-Throughput Screening of Stable Single-Atom Catalysts in CO_2 Reduction Reactions. *ACS Catal.* **2022,** *12*, 8269-8278.
50. Feng, Y.; An, W.; Wang, Z.; Wang, Y.; Men, Y.; Du, Y., Electrochemical CO_2 Reduction Reaction on M@Cu(211) Bimetallic Single-Atom Surface Alloys: Mechanism, Kinetics, and Catalyst Screening. *ACS Sustainable Chem. Eng.* **2020,** *8*, 210-222.
51. Liu, T.; Wang, Q.; Wang, G.; Bao, X., Electrochemical CO_2 Reduction on Graphdiyne: A DFT Study. *Green Chem.* **2021,** *23*, 1212-1219.

52. Mou, S.; Wu, T.; Xie, J.; Zhang, Y.; Ji, L.; Huang, H.; Wang, T.; Luo, Y.; Xiong, X.; Tang, B.; Sun, X., Boron Phosphide Nanoparticles: A Nonmetal Catalyst for High-Selectivity Electrochemical Reduction of CO_2 to CH_3OH. *Adv. Mater.* **2019,** *31*, 1903499.

53. Chen, H.; Fan, T.; Ji, Y., CO_2 Reduction Mechanism on the $Cu_2O(110)$ Surface: A First-Principles Study. *ChemPhysChem* **2023,** *24*, e202300047.

54. Darby, M. T.; Sykes, E. C. H.; Michaelides, A.; Stamatakis, M., Carbon Monoxide Poisoning Resistance and Structural Stability of Single Atom Alloys. *Top. Catal.* **2018,** *61*, 428-438.

55. Lu, S.; Zhou, Q.; Ouyang, Y.; Guo, Y.; Li, Q.; Wang, J., Accelerated Discovery of Stable Lead-Free Hybrid Organic-Inorganic Perovskites via Machine Learning. *Nat. Commun.* **2018,** *9*, 3405.

56. Greiner, M. T.; Jones, T. E.; Beeg, S.; Zwiener, L.; Scherzer, M.; Girgsdies, F.; Piccinin, S.; Armbrüster, M.; Knop-Gericke, A.; Schlögl, R., Free-Atom-Like *d* States in Single-Atom Alloy Catalysts. *Nat. Chem.* **2018,** *10*, 1008-1015.

57. Spivey, T. D.; Holewinski, A., Selective Interactions between Free-Atom-like *d*-States in Single-Atom Alloy Catalysts and Near-Frontier Molecular Orbitals. *J. Am. Chem. Soc.* **2021,** *143*, 11897-11902.

58. Fung, V.; Hu, G.; Wu, Z.; Jiang, D.-e., Descriptors for Hydrogen Evolution on Single Atom Catalysts in Nitrogen-Doped Graphene. *J. Phys. Chem. C* **2020,** *124*, 19571-19578.

59. Taunk, K.; De, S.; Verma, S.; Swetapadma, A. In *A Brief Review of Nearest Neighbor Algorithm for Learning and Classification*, 2019 International Conference on Intelligent Computing and Control Systems (ICCS), 15-17 May 2019; 2019; pp 1255-1260.

60. Wu, Z.; Liu, J.; Mu, B.; Xu, X.; Sheng, W.; Tao, W.; Li, Z., Machine-Learning Assisted Screening of Double Metal Catalysts for CO_2 Electroreduction to CH_4. *Appl. Surf. Sci.* **2024,** *648*, 159027.

61. Davies, D. W.; Butler, K. T.; Walsh, A., Data-Driven Discovery of Photoactive Quaternary Oxides Using First-Principles Machine Learning. *Chem. Mater.* **2019,** *31*, 7221-7230.